Title

A laser-assisted chlorination process for reversible writing of doping patterns in graphene

Journal

Nature Electronics, 5(8)

ISSN

2520-1131

Authors

Rho, Yoonsoo

Lee, Kyunghoon

Wang, Letian

et al.

Publication Date

2022-08-01

DOI

10.1038/s41928-022-00801-2

nature electronics

ARTICLES

https://doi.org/10.1038/s41928-022-00801-2

Check for updates

A laser-assisted chlorination process for reversible writing of doping patterns in graphene

Yoonsoo Rho[1,10], Kyunghoon Lee[2,10], Letian Wang[1], Changhyun Ko[3,4], Yabin Chen[3,5], Penghong Ci[3,6], Jiayun Pei[1,7], Alex Zettl[2,8,9], Junqiao Wu[3] and Costas P. Grigoropoulos[1]✉

Chemical doping can be used to control the charge-carrier polarity and concentration in two-dimensional van der Waals materials. However, conventional methods based on substitutional doping or surface functionalization result in the degradation of electrical mobility due to structural disorder, and the maximum doping density is set by the solubility limit of dopants. Here we show that a reversible laser-assisted chlorination process can be used to create high doping concentrations (above 3×10^{13} cm^{-2}) in graphene monolayers with minimal drops in mobility. The approach uses two lasers—with distinct photon energies and geometric configurations—that are designed for chlorination and subsequent chlorine removal, allowing highly doped patterns to be written and erased without damaging the graphene. To illustrate the capabilities of our approach, we use it to create rewritable photoactive junctions for graphene-based photodetectors.

Chemical doping using methods such as substitutional doping[1–4] and chemical surface functionalization via the covalent bonding of adsorbed molecules[5,6] is commonly used to control the sign and concentration of carriers in two-dimensional (2D) van der Waals materials. However, high carrier concentrations are restricted by the solubility limit of the dopant[1–4] and charge mobilities are impaired by structural disorder that is inevitably introduced by covalent bonding[1–4,7]. Electrostatic gating[8,9] and trapped charge in dielectric layers in a heterostructure[10,11] can externally modulate charge carriers without degrading electrical mobility, but dielectric breakdown imposes fundamental limitations on the doping density. In addition, the lithography processes required to form spatially confined gate circuitry, or the use of a heterostructure, complicates device fabrication. Electrochemical techniques—including chemical intercalation[12,13] and electrolyte gating[14,15]—have been used to achieve impressive doping concentrations, but challenges related to practical device implementation and the degradation of charge mobility by unwanted electrochemical reactions[14,15] remain with such methods.

A promising alternative doping scheme, which is non-invasive, is surface functionalization via non-covalent bonding[16,17]. One such system is chlorinated graphene (which has an ideal chlorine coverage ratio of Cl_2C) where charge transfer between chlorine atoms and graphene can occur via ionic bonding[18,19]. Graphene chlorination offers potential advantages over surface functionalization via hydrogenation and fluorination, where the adsorption of hydrogen and fluorine inevitably forms sp^3-type carbon–hydrogen and carbon–fluorine covalent bonding that degrades the charge-carrier mobility[20,21]. The ionic bonding of chlorine with graphene could also make the doping process reversible[22–24]; therefore, doping patterns can, in principle, be written and erased.

Chlorination via photochemical[24,25] and plasma treatments[22,23,26,27] have previously shown high coverage of chlorine on graphene, suggesting the possibility of creating heavily doped graphene devices that exhibit high performance. However, direct light illumination in the presence of Cl_2 can induce an insulating state[25] or morphological corrugations[24], which limit charge-carrier mobility, and the high momentum of chlorine radicals in the plasma treatment of graphene can create defects unless the plasma power is carefully regulated[22,26] or a metal grid[23,27] is applied to decelerate their momentum. Furthermore, the required simultaneous use of a photoresist process to generate doped patterns could impair the chemical binding state of dopants. It also makes the approach unsuitable for applications that require rewritable patterns.

In this Article, we report a tunable and reversible graphene doping method that is based on laser-assisted chlorination. The chlorination and chlorine removal of graphene is controlled using two separate laser processes with different photon energies and geometric configurations. Due to the saturable and non-invasive characteristics of doping via chlorination, the method can induce high doping densities for device implementation, as well as offering reversibility and spatial selectivity. We show that our approach can create doping concentrations of at least 3×10^{13} cm^{-2} in monolayer graphene at room temperature and causing a minimal mobility decrease (from 4,698 cm^2 V^{-1} s^{-1} in the pristine state to 2,551 cm^2 V^{-1} s^{-1} in the highest-doped state). Subsequent non-invasive chlorine desorption by photothermal laser annealing allows highly doped patterns to be written in graphene. To illustrate the capabilities of this approach, we use it to create rewritable photoactive pixels for graphene photodetectors.

Electrical performance of chlorinated graphene

The experimental scheme for laser-assisted chlorination is illustrated in Fig. 1a. We utilized an ultraviolet (UV) nanosecond laser beam (wavelength $\lambda = 213$ nm (5.8 eV)), which is aligned parallel to

[1]Laser Thermal Laboratory, Department of Mechanical Engineering, University of California, Berkeley, CA, USA. [2]Department of Physics, University of California, Berkeley, CA, USA. [3]Department of Materials Science & Engineering, University of California, Berkeley, CA, USA. [4]Department of Applied Physics, Sookmyung Women's University, Seoul, Republic of Korea. [5]School of Aerospace Engineering, Beijing Institute of Technology, Beijing, People's Republic of China. [6]Institute for Advanced Study, Shenzhen University, Guangdong, People's Republic of China. [7]Department of Mechanical Engineering, Tsinghua University, Beijing, People's Republic of China. [8]Materials Sciences Division, Lawrence Berkeley National Laboratory, Berkeley, CA, USA. [9]Kavli Energy NanoSciences, Institute at the University of California, Berkeley, CA, USA. [10]These authors contributed equally: Yoonsoo Rho, Kyunghoon Lee. ✉e-mail: cgrigoro@berkeley.edu

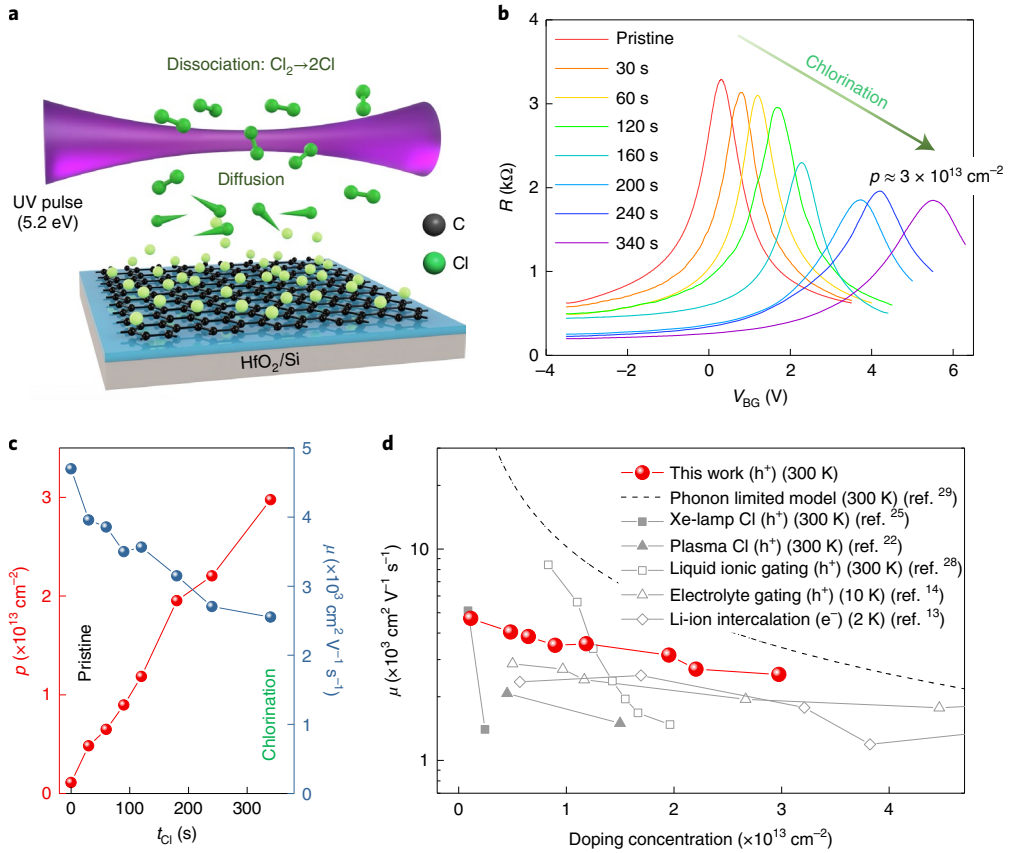

Fig. 1 | Schematic of laser-assisted surface functionalization by chlorine and demonstration of a high doping concentration and high mobility. **a**, Schematic depicting the UV nanosecond laser irradiation in the parallel direction for Cl radical generation. **b**, Transfer curves of graphene FET on HfO_2 (20 nm)/Si wafer in the pristine state and after chlorination for various processing times ranging from 30 to 340 s. **c**, Hole doping concentration p and mobility μ extracted from electrical transfer curves shown in **b** depending on the processing times. **d**, Plots of doping concentration and mobility μ of this work (hole) measured at 300 K and previous works. The data were extracted from the following references: phonon-limited theoretical model[29], xenon-lamp-assisted Cl doping (hole) at 300 K (ref. [25]), Cl plasma treatment (hole) at 300 K (ref. [22]), liquid ionic gating (hole) at 300 K (ref. [28]), electrolyte gating (hole) at 10 K (ref. [14]) and lithium-ion intercalation (electron) at 2 K (ref. [13]).

the sample surface under flowing Cl_2 gas. The Cl_2 molecules can be photochemically dissociated by the focused UV pulsed laser, and the generated Cl radicals diffuse to graphene. First, we used a graphene field-effect transistor (FET) to explicitly determine the carrier density and mobility induced by laser-assisted chlorination. The device was prepared based on mechanically exfoliated monolayer graphene on 20-nm-thick high-κ (dielectric constant $\kappa \approx 20$) HfO_2 grown on a Si wafer to access an ultrahigh-doped state, whereas a conventional SiO_2 dielectric layer has limited access to the doping concentration ($\sim 6 \times 10^{12}\,cm^{-2}$) set by dielectric breakdown (Supplementary Fig. 1). We performed four-terminal measurements under a high vacuum ($<10^{-6}$ torr) at room temperature. As the doping time increased, its charge-neutrality point, V_{CNP}, monotonically shifted to +5.6 V, indicating an ultrahigh p-type doping concentration ($p > 3 \times 10^{13}\,cm^{-2}$). Meanwhile, hole mobility (μ_H) decreased moderately from $4{,}698\,cm^2\,V^{-1}\,s^{-1}$ (pristine) to $2{,}551\,cm^2\,V^{-1}\,s^{-1}$ (doped state at $\sim 3 \times 10^{13}\,cm^{-2}$), which was attributed to increased carrier scattering (Fig. 1b, c). We note that the measurement of a higher doping concentration beyond this point was limited by the dielectric breakdown of the HfO_2 layer, and therefore, the presented doping density is a lower-bound limit. Despite the constraint, our result showed a higher doping concentration and charge-carrier mobility than liquid ionic gating[28], xenon-lamp-induced Cl doping[25] and Cl plasma treatment[22], whereas in the high-doping-density regime, it presented charge mobility closer to the theoretical limit imposed by phonon scattering (Supplementary Note 2)[29] compared with other state-of-the-art doping methods, including lithium-ion intercalation[13] and electrolyte gating[14] (Fig. 1d).

Raman and XPS analyses of chlorinated graphene

The presented high carrier density with high mobility implies that the laser-assisted chlorination process takes full advantage of the non-invasive bonding characteristics of chlorinated graphene. To understand the chemical trend in doping, we carried out Raman and X-ray photoelectron spectroscopy (XPS) analyses based on mechanically exfoliated monolayer graphene on a SiO_2 (300 nm)/Si wafer (Fig. 2). Raman spectra near the G and 2D peaks (Fig. 2a) showed that both peaks blueshifted from 1,584 and 2,678 cm^{-1} to 1,600 and 2,689 cm^{-1}, respectively, whereas the I_{2D}/I_G intensity ratio decreased from 2.8 to 1.0, indicating a strong p-type doping effect[30,31] (Fig. 2a,b). Additionally, no sign of defects (for example, D peak ($\sim$1,350 cm^{-1})) was observed (Supplementary Fig. 4 shows the full spectra). As described in Fig. 2b, the changes in the Raman spectra showed a monotonic shift and saturation after 5 min. We note that this trend contrasts with previous reports on chlorination by plasma treatment, wherein an excessive processing time decreased the doping density[22]. We attribute this difference to the low momentum energy of Cl radicals generated by the laser, due to the short mean free path of Cl atoms ($\sim$100 nm in the limit of the ideal gas approximation at 400 torr (ref. [32])), as well as the absence of an external driving force such as an electric field. The UV nanosecond laser in the parallel direction can excite the Cl_2 electronic

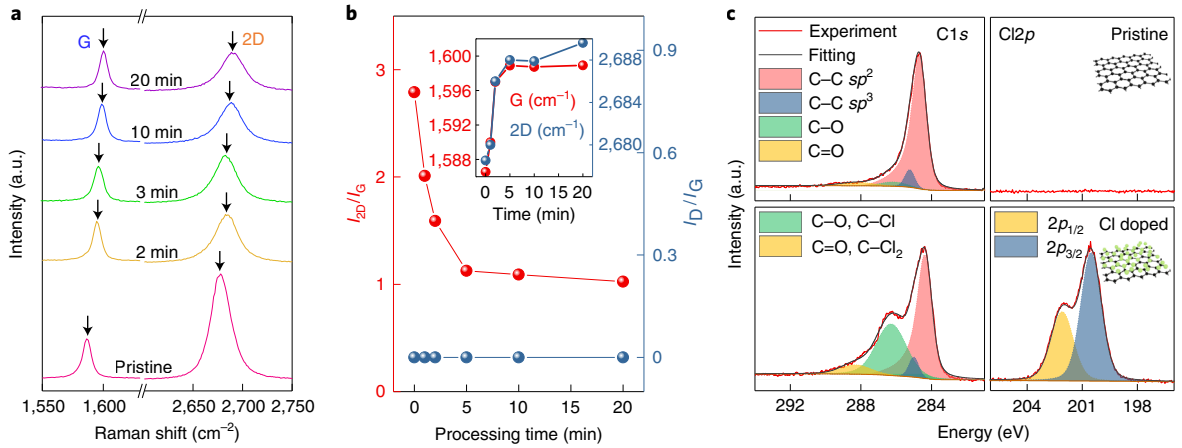

Fig. 2 | Non-invasive and saturable characteristics of the chlorination process. a, Raman spectra near the G and 2D peaks of pristine and chlorinated graphene monolayers at various doping times. **b**, Plot of chlorination time versus Raman I_{2D}/I_G ratio, I_D/I_G ratio, and G and 2D peak positions (inset). **c**, XPS spectra obtained from pristine (top row) and chlorinated (bottom row) graphene near the C1s (left) and Cl2*p* (right) peaks. The curves obtained by peak deconvolution, based on the method described elsewhere[47], are overlaid.

energy state (ground state ($^1\Sigma_g$)→excited state ($^1\Pi_u$)) and break Cl_2 bonding[33,34] without affecting the surface. The generated Cl radicals diffuse to the graphene surface and experience substantial momentum reduction.

XPS analysis also revealed clear evidence of the high coverage of chlorine without structural damage (Fig. 2c). We utilized chemical vapour deposition (CVD)-grown graphene for XPS analysis to accommodate relatively large X-ray focal spots (~100 μm). As presented in the C1*s* XPS spectra of pristine graphene, a narrow asymmetric shape was clearly observed, representing graphene's sp^2 C–C bonding peak (at 284.5 eV)[35,36]. Meanwhile, the contributions of the oxidized carbon bonding and sp^3 C–C bonding at 285.2 eV (~10% area) cannot be ignored due to the intrinsic defects of CVD graphene. After the chlorination process, C–Cl (286.2 eV) and C–Cl_2 (288.3 eV) bonding states were evident, which overlapped with the C–O and C=O peaks, respectively[36], and a portion of the sp^3 C–C bonding was maintained. In addition, the Cl2*p* peak was observed after doping, evidencing the introduction of chlorine. The C–Cl elemental ratio was estimated to be 43.5% based on the intensity of the C and Cl peaks, which is close to the values achieved by plasma treatment[22,26] (Supplementary Note 7). However, we note that the observed high Cl coverage ratio in graphene deviates from the theoretical prediction based on free-standing graphene[18]: a maximum of 12.5% Cl coverage ratio was predicted as stable stoichiometry in chlorinated graphene when it forms ionic bonding by the charge transfer complex. A higher coverage ratio exceeding this value would result in a weaker non-invasive bonding state, termed 'non-bonding', where Cl probably escapes from graphene by forming Cl_2 molecules due to the weak interaction between Cl and graphene. Meanwhile, a recent experimental study on the chlorination of graphene by plasma doping suggested a potential substrate effect by showing changes in the maximum Cl coverage ratio depending on the type of substrate (dielectric or metal)[26]. This result implies that the substrate may affect the Cl–graphene interaction, which induced the observed unexpectedly high Cl coverage ratio.

Based on the suggested Cl-binding mechanisms, we obtained the theoretically estimated doping concentration in graphene. The charge transfer rate between Cl and graphene is small in the case of a non-bonding state (0.03 hole per single Cl) due to the weak interaction[18]. Considering the carbon density of graphene ($3.82\times10^{15}\,cm^{-2}$), in the case of the C_2Cl ratio, charge density p can be as high as $5.73\times10^{13}\,cm^{-2}$, despite the small charge transfer rate. In the case of ionic bonding (charge transfer complex), which can induce 12.5% of the maximum Cl coverage ratio (C_8Cl), the charge transfer rate is 0.27 hole per Cl (ref. [18]), which can result in $p=1.27\times10^{14}\,cm^{-2}$. Thus, we expect that the combination of non-bonding and ionic bonding states of Cl can readily induce the experimentally observed high doping concentration.

Site-selective chlorine removal process

The Cl dopant can be reversibly removed by a photothermal process. We introduced a continuous-wave (CW) green laser ($\lambda=532$ nm (2.3 eV)) in the normal direction with a focal size of 2 μm ($1/e^2$) (Fig. 3a). After Cl removal by laser irradiation (25 mW and 1 min), the G and 2D Raman peaks downshifted to 1,588 and 2,677 cm^{-1}, respectively, and the I_{2D}/I_G intensity ratio was restored to 2.5 without D-peak generation, similar to the pristine graphene state, whereas we observed Raman G-peak splitting due to local doping variation (Supplementary Note 9). By a subsequent rechlorination process, the hole-doped state was uniformly restored over the entire graphene sheet (Fig. 3b). Based on this procedure, arbitrary doped patterns can be reversibly formed without defects (Fig. 3f). To elucidate the effect of the CW green laser in the Cl removal process, we carried out heat transfer simulation and Kelvin probe force microscopy (KPFM) mapping. KPFM mapping was performed to resolve the spatial distribution of changes in the chemical potential of graphene due to the removal of Cl beyond the optical diffraction limit of Raman probing. From the simulated temperature profile (Fig. 3c), the full-width at half-maximum of the developed steady-state temperature profile on graphene was estimated to be ~1.2 μm. Meanwhile, the KPFM images obtained from the Cl^--removed spot (Fig. 3d) showed a wider distribution (~1.7 μm, at 25 mW for 1 min), as depicted by plotting the line profile overlaid on the temperature distribution induced by the laser (Fig. 3e). This trend suggests that the laser-induced Cl desorption was dominated by thermal processes. Photochemical routes typically tend to generate features smaller than the size of the Gaussian-profile laser-beam focal spot[34,37].

Demonstration of rewritable photoactive junctions

Such rewritable and highly doped patterns in graphene can demonstrate the writing and erasure of photoactive junctions in graphene-based photodetectors (Fig. 4a). We utilized a hexagonal boron nitride (hBN)/SiO_2 (300 nm) dielectric layer and applied the chlorination condition for a large doping concentration (~$10^{13}\,cm^{-2}$) (Supplementary Note 14). In photocurrent mapping, a CW laser

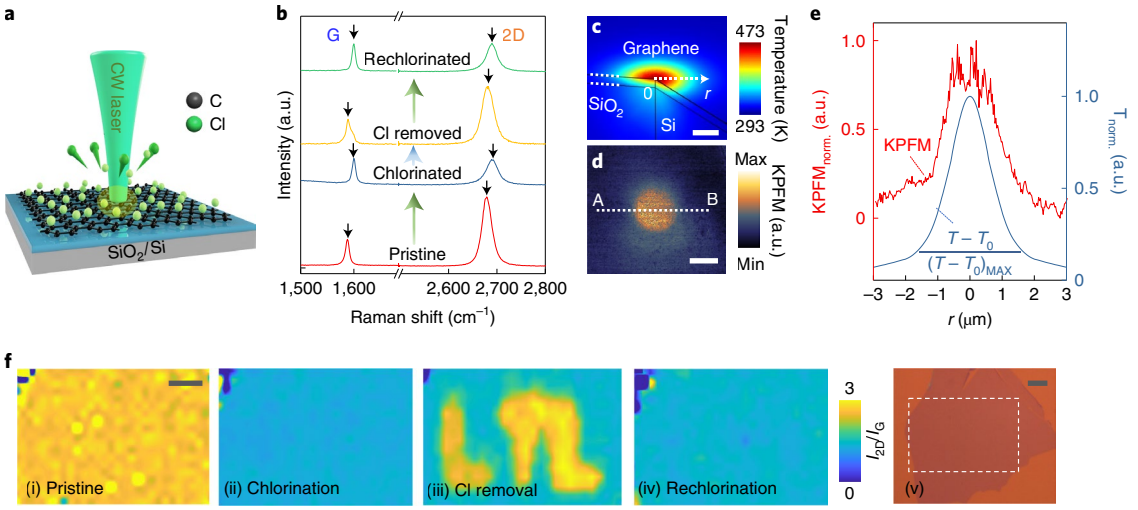

Fig. 3 | Reversible chlorine removal process by CW green laser. a, Schematic depicting the site-selective reversible Cl removal by irradiation with CW green laser in the normal direction. **b**, Raman spectra near the G and 2D peaks of pristine, chlorinated, Cl removed and rechlorinated graphene monolayers. **c**, Steady-state temperature profile of the graphene/SiO_2 (300 nm)/Si structure under the illumination of 35 mW of laser power. **d**, KPFM image obtained from the Cl removed area. Scale bars, 1 μm (**c** and **d**). **e**, Normalized temperature profiles $(T-T_0)/(T-T_0)_{MAX}$, where T_0 is the initial temperature, along the *r* direction from the centre of graphene in **c** and normalized KPFM values along the A–B line in **d**. **f**, Raman I_{2D}/I_G maps of graphene at various processing states ((i)–(iv)). After reversible chlorine removal in the designed patterns, 'LTL' (referring to Laser Thermal Laboratory) are evident in the Raman maps (iii). Optical microscopy image of graphene (v). The white dashed box indicates the Raman mapping region. Scale bars, 4 μm (**f**).

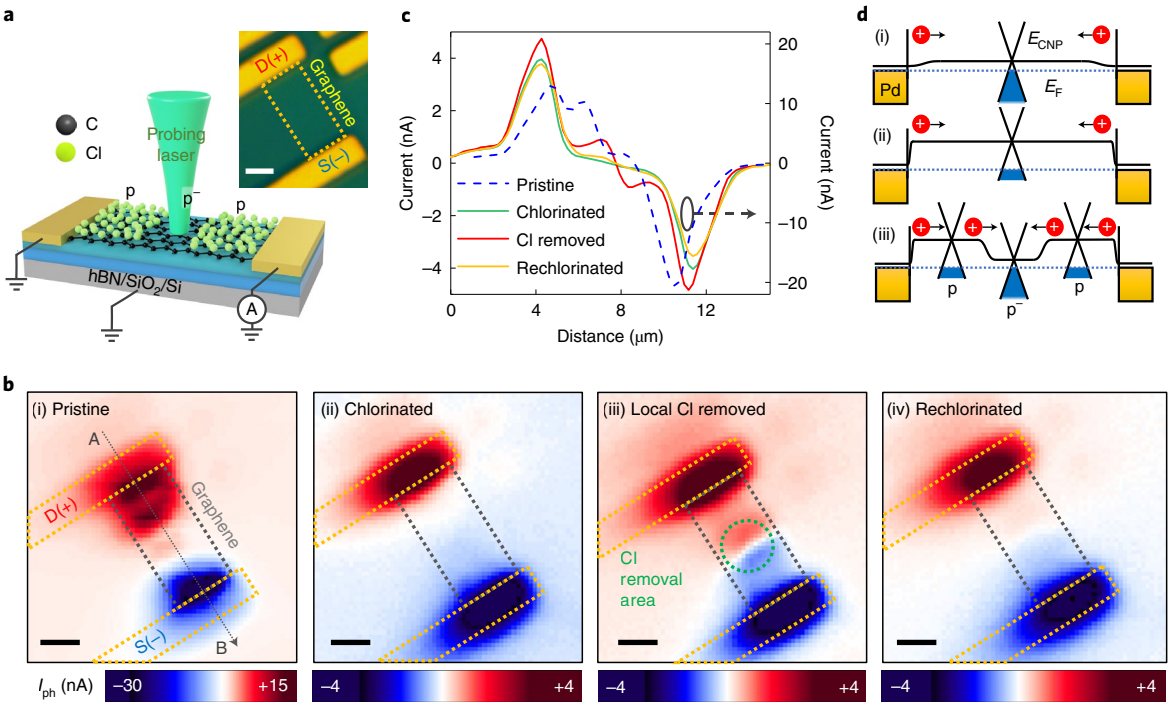

Fig. 4 | Demonstration of rewritable photoactive junction using chlorination and local chlorine removal processes. a, Schematic of the photocurrent mapping setup and optical microscopy image of a real device prepared on hBN/SiO_2 (300 nm) dielectric layer. **b**, Photocurrent mapping images of pristine (i), chlorinated (ii), local Cl removed (iii) and rechlorinated (iv) graphene photodetectors. The green circle in (iii) indicates the area where the CW laser irradiated for the Cl removal process. Scale bars, 2 μm (**a** and **b**). **c**, Line profiles of photocurrent across the device (metal–graphene–metal along the A–B line in **b**(i)) at each processing step obtained from the photocurrent maps in **b**. **d**, Energy-band diagrams of the graphene device and direction of photocurrent at junctions in the pristine (i), chlorinated (ii) and local Cl removed (iii) states.

beam (532 nm) with a 1 μm ($1/e^2$) spot size at 100 μW power was raster scanned and the source–drain current (I_{ph}) was collected at zero source–drain voltage (V_{sd}) and grounded gate voltage (V_g). The positive current indicates the excited hole moving towards the source. As shown in Fig. 4b(i), pristine graphene showed a substantial photocurrent at the metal/graphene junctions in opposite polarities due to the built-in potential developed by Fermi-level pinning[38]. Furthermore, an irregular photocurrent appears at the

graphene channel area, attributed to the local electron–hole puddle. After the chlorination process (Fig. 4b(ii)), the photocurrent in the channel area was eliminated as the high doping concentration overwhelmed any non-uniform doping fluctuation in graphene. Additionally, the distance between the photocurrent peaks that appeared at the two opposite metal/graphene junctions of the chlorinated device increased to 7.1 μm, whereas in its pristine state, this was 5.8 μm (Fig. 4c). The high doping concentration caused sharp band bending near the electrodes, and the peak position of the photocurrent shifted towards the metal[38,39]. After local Cl removal at the centre of the channel area, the photocurrent clearly appeared in a symmetric distribution of opposite polarities (Fig. 4b(iii)). The formation of p–p$^-$–p junctions in the graphene channel resulted in opposite band bending (Fig. 4d(iii)).

We attribute the observed photocurrent in the channel area to the photothermoelectric (PTE) effect, which originates from the local non-uniformity in the Seebeck coefficient modulated by the gradient of the density of states, represented by the Mott formula[9,40]. It has been reported that the PTE effect at graphene unipolar junctions (that is, p–p$^-$ or n–n$^-$ junctions) imposes photocurrent directions opposite to the photovoltaic (PV) effect[9], where the excited charges are drifted by the built-in chemical potential. Considering the chemical potentials developed in p–p$^-$–p junctions (Fig. 4d), if the PV effect dominates the photocurrent, the photocurrent should flow in opposite directions to our experimental results, implying that the observed photocurrent at doped junctions is driven by the PTE effect. Moreover, the calculated ratio ($I_{PTE}/I_{PV} \approx 5$) between the PTE (I_{PTE})- and PV (I_{PV})-induced currents[41,42] at our p–p$^-$ junction also indicated that the PTE effect was dominant across the overall signal (Supplementary Note 15). On the other hand, at the metal/graphene junction, the photocurrent mechanism cannot be solely differentiated by its flow direction, as the photocurrents by both PV and PTE effects have the same direction[43,44] (Supplementary Note 16).

Next, the rechlorination process can reversibly erase the photocurrent junction formed at the channel area, and the photodetector is ready for the generation of a new photoactive pixel (Fig. 4b(iv)). The line profiles of the photocurrent maps show identical shapes in the chlorinated and rechlorinated states of the photodetector (Fig. 4c). Thus, this result shows that the developed laser-assisted reversible chlorination mechanism enables rewritable photoactive pixels in graphene photodetectors.

Conclusions

We have reported the reversible doping of graphene using laser-assisted surface functionalization by chlorine. A UV nanosecond laser in the parallel direction is used to achieve saturable ultrahigh-doping concentrations (a lower bound of 3×10^{13} cm^{-2}) and creating a minimal drop in the carrier mobility (from 4,698 cm^2 V^{-1} s^{-1} in the pristine state to 2,551 cm^2 V^{-1} s^{-1} in the highest-doped state). A CW green laser in the normal direction can be subsequently used to induce local chlorine removal, allowing highly doped patterns to be written and erased. Raman and XPS measurements showed that the chlorination and chlorine removal processes do not result in structural damage to the graphene. Furthermore, we used this method to create rewritable photoactive pixels in a graphene photodetector.

Our approach is distinct from previously reported laser-assisted chemical processing techniques for 2D van der Waals materials, which rely on the direct illumination of a single laser beam at the doping source[45,46] and induce unintentional chemical reactions that can degrade mobility and limit the doping concentration (Supplementary Note 18). Our two-laser-beam-assisted surface functionalization approach could allow various dopant elements to be incorporated into 2D van der Waals materials and thus the writing of local electronic functionalities for multiple optoelectronic applications.

Methods

Preparation of monolayer graphene flakes. We utilized both mechanically exfoliated and CVD-grown graphene monolayers. The exfoliated graphene was used for Raman analysis, KPFM and FET device fabrication, whereas CVD graphene was employed for XPS analysis.

Chlorination and Cl removal processes. The as-prepared graphene monolayer was placed in a laser chemical processing chamber equipped with quartz windows for access to laser beams from various geometric configurations. Here 1% Cl_2 was diluted in He flows at 50 s.c.c.m. at controlled pressure (400 torr). The parallel irradiated UV nanosecond laser beam (4 mJ; $\lambda = 213$ nm (5.8 eV); pulse width, ~16 ns; 11 Hz repetition rate) was focused at 500 μm above the graphene surface through a spherical lens ($f \approx 100$ mm). For the Cl removal process, a CW laser ($\lambda = 532$ nm (2.3 eV)) was focused by an objective lens (numerical aperture, 0.55) on graphene under ambient conditions.

Raman, KPFM and XPS characterizations. Graphene samples for Raman, KPFM and XPS characterizations were prepared on SiO_2 (300 nm)/Si wafers. A Raman spectroscopy system equipped with a 532 nm excitation laser beam source at 0.5 mW and 1,800 lines per mm grating (Renishaw) was utilized. KPFM mapping was conducted by an atomic force microscopy system (VistaScope, Molecular Vista), and Supplementary Note 13 provides details of the electrical setup. XPS analysis was performed using a PHI 5600 XPS apparatus.

Heat transfer analysis. Supplementary Note 12 provides the details.

Device fabrication and measurement. The mechanically exfoliated graphene monolayer was dry transferred onto HfO_2/Si. Using electron-beam lithography, the shape and dimensions of graphene and palladium electrodes were defined, followed by oxygen-plasma etching and lift-off processes, respectively. All the FET device characterizations were performed with four-terminal measurements at a high vacuum (3×10^{-8} torr) and room temperature. Supplementary Note 3 provides details of the fitting of the electrical transport curve.

Photocurrent measurement. The photocurrent device was prepared by the same procedure used for FET device fabrication, except for the use of ~20 nm hBN flake and SiO_2 (300 nm)/Si wafer. A CW 532 nm laser was mechanically chopped at 730 Hz. The source–drain voltage was zero, and the back gate was grounded. The generated photocurrent was filtered at 730 Hz using a lock-in amplifier.

Data availability

The data supporting the plots within this paper are available via Zenodo at https://doi.org/10.5281/zenodo.6655757.

Received: 17 August 2021; Accepted: 22 June 2022;
Published online: 01 August 2022

References

1. Lv, R. et al. Ultrasensitive gas detection of large-area boron-doped graphene. *Proc. Natl Acad. Sci. USA* **112**, 14527–14532 (2015).
2. Wang, H., Maiyalagan, T. & Wang, X. Review on recent progress in nitrogen-doped graphene: synthesis, characterization, and its potential applications. *ACS Catal.* **2**, 781–794 (2012).
3. Chaban, V. V. & Prezhdo, O. V. Boron doping of graphene—pushing the limit. *Nanoscale* **8**, 15521–15528 (2016).
4. Zhang, K. et al. Tuning the electronic and photonic properties of monolayer MoS_2 via in situ rhenium substitutional doping. *Adv. Funct. Mater.* **28**, 1706950 (2018).
5. Niyogi, S. et al. Spectroscopy of covalently functionalized graphene. *Nano Lett.* **10**, 4061–4066 (2010).
6. Makarova, M., Okawa, Y. & Aono, M. Selective adsorption of thiol molecules at sulfur vacancies on MoS_2 (0001), followed by vacancy repair via S–C dissociation. *J. Phys. Chem. C* **116**, 22411–22416 (2012).
7. Sarkar, S., Bekyarova, E. & Haddon, R. C. Covalent chemistry in graphene electronics. *Mater. Today* **15**, 276–285 (2012).
8. Novoselov, K. S. et al. Electric field effect in atomically thin carbon films. *Science* **306**, 666–669 (2004).
9. Gabor, N. M. et al. Hot carrier–assisted intrinsic photoresponse in graphene. *Science* **334**, 648–652 (2011).
10. Ju, L. et al. Photoinduced doping in heterostructures of graphene and boron nitride. *Nat. Nanotechnol.* **9**, 348–352 (2014).
11. Shi, W. et al. Reversible writing of high-mobility and high-carrier-density doping patterns in two-dimensional van der Waals heterostructures. *Nat. Electron.* **3**, 99–105 (2020).
12. Bediako, D. K. et al. Heterointerface effects in the electrointercalation of van der Waals heterostructures. *Nature* **558**, 425–429 (2018).
13. Zhao, S. F. et al. Controlled electrochemical intercalation of graphene/h-BN van der Waals heterostructures. *Nano Lett.* **18**, 460–466 (2017).

14. Efetov, D. K. & Kim, P. Controlling electron-phonon interactions in graphene at ultrahigh carrier densities. *Phys. Rev. Lett.* **105**, 256805 (2010).
15. Ovchinnikov, D. et al. Disorder engineering and conductivity dome in ReS_2 with electrolyte gating. *Nat. Commun.* **7**, 12391 (2016).
16. Georgakilas, V. et al. Noncovalent functionalization of graphene and graphene oxide for energy materials, biosensing, catalytic, and biomedical applications. *Chem. Rev.* **116**, 5464–5519 (2016).
17. Baltazar, J. et al. Photochemical doping and tuning of the work function and Dirac point in graphene using photoacid and photobase generators. *Adv. Funct. Mater.* **24**, 5147–5156 (2014).
18. Yang, M., Zhou, L., Wang, J., Liu, Z. & Liu, Z. Evolutionary chlorination of graphene: from charge-transfer complex to covalent bonding and nonbonding. *J. Phys. Chem. C* **116**, 844–850 (2012).
19. Sahin, H. & Ciraci, S. Chlorine adsorption on graphene: chlorographene. *J. Phys. Chem. C* **116**, 24075–24083 (2012).
20. Robinson, J. T. et al. Properties of fluorinated graphene films. *Nano Lett.* **10**, 3001–3005 (2010).
21. Elias, D. C. et al. Control of graphene's properties by reversible hydrogenation: evidence for graphane. *Science* **323**, 610–613 (2009).
22. Zhang, X. et al. Impact of chlorine functionalization on high-mobility chemical vapor deposition grown graphene. *ACS Nano* **7**, 7262–7270 (2013).
23. Pham, V. P., Kim, K. N., Jeon, M. H., Kim, K. S. & Yeom, G. Y. Cyclic chlorine trap-doping for transparent, conductive, thermally stable and damage-free graphene. *Nanoscale* **6**, 15301–15308 (2014).
24. Copetti, G. et al. Reversibility of graphene photochlorination. *J. Phys. Chem. C* **122**, 16333–16338 (2018).
25. Li, B. et al. Photochemical chlorination of graphene. *ACS Nano* **5**, 5957–5961 (2011).
26. Zhang, X. et al. X-ray spectroscopic investigation of chlorinated graphene: surface structure and electronic effects. *Adv. Funct. Mater.* **25**, 4163–4169 (2015).
27. Pham, V. P. et al. Low damage pre-doping on CVD graphene/Cu using a chlorine inductively coupled plasma. *Carbon* **95**, 664–671 (2015).
28. Ye, J. et al. Accessing the transport properties of graphene and its multilayers at high carrier density. *Proc. Natl Acad. Sci. USA* **108**, 13002–13006 (2011).
29. Hwang, E. & Sarma, S. D. Acoustic phonon scattering limited carrier mobility in two-dimensional extrinsic graphene. *Phys. Rev. B* **77**, 115449 (2008).
30. Das, A. et al. Monitoring dopants by Raman scattering in an electrochemically top-gated graphene transistor. *Nat. Nanotechnol.* **3**, 210–215 (2008).
31. Ferrari, A. C. Raman spectroscopy of graphene and graphite: disorder, electron–phonon coupling, doping and nonadiabatic effects. *Solid State Commun.* **143**, 47–57 (2007).
32. Carey, V. P. *Statistical Thermodynamics and Microscale Thermophysics* (Cambridge Univ. Press, 1999).
33. Heaven, M. C. & Clyne, M. A. A. Interpretation of the spontaneous predissociation of $Cl_2[B^3\Pi(0^+_u)]$. *J. Chem. Soc., Faraday Trans. 2* **78**, 1339–1344 (1982).
34. Bäuerle, D. W. *Laser Processing and Chemistry* (Springer, 2011).
35. Moeini, B. et al. Definition of a new (Doniach-Sunjic-Shirley) peak shape for fitting asymmetric signals applied to reduced graphene oxide/graphene oxide XPS spectra. *Surf. Interface Anal.* **54**, 67–77 (2021).
36. Stöhr, J. *NEXAFS Spectroscopy* (Springer Science & Business Media, 1992).
37. Grigoropoulos, C. P. *Transport in Laser Microfabrication: Fundamentals and Applications* (Cambridge Univ. Press, 2009).
38. Mueller, T., Xia, F., Freitag, M., Tsang, J. & Avouris, P. Role of contacts in graphene transistors: a scanning photocurrent study. *Phys. Rev. B* **79**, 245430 (2009).
39. Xia, F. et al. Photocurrent imaging and efficient photon detection in a graphene transistor. *Nano Lett.* **9**, 1039–1044 (2009).
40. Hwang, E., Rossi, E. & Sarma, S. D. Theory of thermopower in two-dimensional graphene. *Phys. Rev. B* **80**, 235415 (2009).
41. De Sanctis, A. et al. Extraordinary linear dynamic range in laser-defined functionalized graphene photodetectors. *Sci. Adv.* **3**, e1602617 (2017).
42. Song, J. C., Rudner, M. S., Marcus, C. M. & Levitov, L. S. Hot carrier transport and photocurrent response in graphene. *Nano Lett.* **11**, 4688–4692 (2011).
43. Echtermeyer, T. J. et al. Photothermoelectric and photoelectric contributions to light detection in metal–graphene–metal photodetectors. *Nano Lett.* **14**, 3733–3742 (2014).
44. Park, J., Ahn, Y. H. & Ruiz-Vargas, C. Imaging of photocurrent generation and collection in single-layer graphene. *Nano Lett.* **9**, 1742–1746 (2009).
45. Kim, E. et al. Site selective doping of ultrathin metal dichalcogenides by laser-assisted reaction. *Adv. Mater.* **28**, 341–346 (2016).
46. Seo, B. H., Youn, J. & Shim, M. Direct laser writing of air-stable p–n junctions in graphene. *ACS Nano* **8**, 8831–8836 (2014).
47. Fairley, N. et al. Systematic and collaborative approach to problem solving using X-ray photoelectron spectroscopy. *Appl. Surf. Sci. Adv.* **5**, 100112 2021).

Acknowledgements

We thank S. Khan, T. Zhu (Department of Physics, UC Berkeley) and J. Park (Department of Mechanical Engineering, Kumoh National Institute of Technology) for useful discussions. Financial support awarded to the University of California, Berkeley, by the US National Science Foundation (grant nos. CMMI-1662475 and CMMI-2024391 (C.P.G.)) is gratefully acknowledged. This work was also partially supported by the Samsung Research Global Outreach (C.P.G). Device fabrication was supported by the Director, Office of Science, Office of Basic Energy Sciences, Materials Sciences and Engineering Division, US Department of Energy, under contract number DE-AC02-05CH11231 (van der Waals heterostructures program (KCWF16)) (A.Z.). The chlorination experiments were conducted at the Laser-Assisted Chemical Vapor Deposition (LACVD) apparatus at UC Berkeley's Marvell Nanofabrication Laboratory.

Author contributions

C.P.G., J.W., Y.R. and K.L. conceived the experiments and idea. C.P.G., Y.R. and L.W. contributed to the development of the laser chemical doping process. A.Z., Y.R., K.L. and C.K. contributed to the device fabrication. Y.R. and K.L. conducted all the device fabrication and measurements. Y.R., Y.C., P.C. and J.P. contributed to the sample preparation and characterization. Y.R., K.L., J.W. and C.P.G. wrote the manuscript, with inputs and comments from all the authors.

Competing interests

The authors declare no competing interests.

Additional information

Supplementary information The online version contains supplementary material available at https://doi.org/10.1038/s41928-022-00801-2.

Correspondence and requests for materials should be addressed to Costas P. Grigoropoulos.

Peer review information *Nature Electronics* thanks Nathaniel Gabor, Cláudio Radtke and the other, anonymous, reviewer(s) for their contribution to the peer review of this work.